A Comparative Study of an Optimal Control Scheme in Different Magnetic Bearings' Geometries

Yago Pessanha Corrêa[1], Laura Julia Martins Mothé[2], Vinícius Ramos Vasco[3], Domingos de Farias Brito David[4], and Afonso Celso Del Nero Gomes[5]

[1] Instituto Federal Fluminense (IFFluminense)
yago.correa@iff.edu.br
[2] Universidade Federal do Rio de Janeiro (UFRJ)
lauramothe@gmail.com
[3] Marinha do Brasil (*Brazilian Navy*)
viniciusramosvasco@gmail.com
[4] Universidade Federal Fluminense (UFF)
domingos@vm.uff.br
[5] Universidade Federal do Rio de Janeiro (UFRJ)
nero@coep.ufrj.br

Abstract

Active Magnetic Bearings (AMB) are devices that support a shaft, showing the advantage of having no contact with any rotating parts, thus eliminating wear and the need of lubrication. Intrinsically, these equipments are unstable and, therefore, a control strategy is necessary in order to stabilize the system. One of the most used state-space feedback method is the Linear Quadratic Regulator (LQR). This paper aims to simulate and compare the eight, four and three-pole AMB with the centralized, decentralized and two-parameter decentralized LQR control strategies. After deducting the reluctance force equations and the system dynamics equations for each of the geometries, several simulations were performed. The results were conclusive and indicated the preference to use the two-parameter decentralized controller, due to the shorter stabilization time and the control variables decoupling, among other factors.

1 Background

Bearings are fixed devices used as a support for rotating axes. Besides that, they allow the relative movement between two surfaces. In a mechanical bearing, due to the contact between the shaft surface and the bearing surface, frictional forces show up. This is a considerable problem as it wears out the machine elements. A possible solution to mitigate this issue is the use of lubricating oils and bushings [1]. In some applications, such as pharmaceutical and food industries, employing general-purpose lubricants is not allowed due to possible contamination [2].

Active Magnetic Bearings (AMB), commonly known as Magnetic Bearings, come as a reasonable solution to overcome the problems presented above. The component's overheating caused by friction is eliminated in this scenario since there is no direct contact between the rotating parts. This type of non-contact bearing is based on the generation of restorative forces caused by electromagnets placed in strategic points. An active control scheme is necessary to stabilize the system considering its inherently unstable feature [3].

Currently, three widespread Magnetic Bearings configurations are addressed in the literature: eight-pole, four-pole and three-pole geometries [4]. In some specific applications, six-pole and twelve-pole bearings can also be used. The differences refer to heat dissipation, energy consumption, manufacturing cost and symmetry [5]. Each of them presents a different modelling

as a result of its own reluctance forces and (un)coupled magnetic fluxes, as will be shown later in this paper.

This work aims to present different comparisons between the eight-pole, four-pole and three-pole geometries of AMBs. In order to carry out the comparative study, three optimal control schemes (all of them based on the Linear Quadratic Regulator approach) will be used – centralized, decentralized and two-parameter decentralized. Simulations are done, and compared in each of the proposed geometries, to visualize if the rotor is kept in the central position when the active control, based on state space analysis, is used.

2 Discussion

The first step in order to compare the geometries is to find the reluctance forces in each possible configuration – i.e., it is necessary to model the system. Consider an 8-pole Magnetic Bearing shown in Figure 1. This configuration is the most used in industrial applications [5].

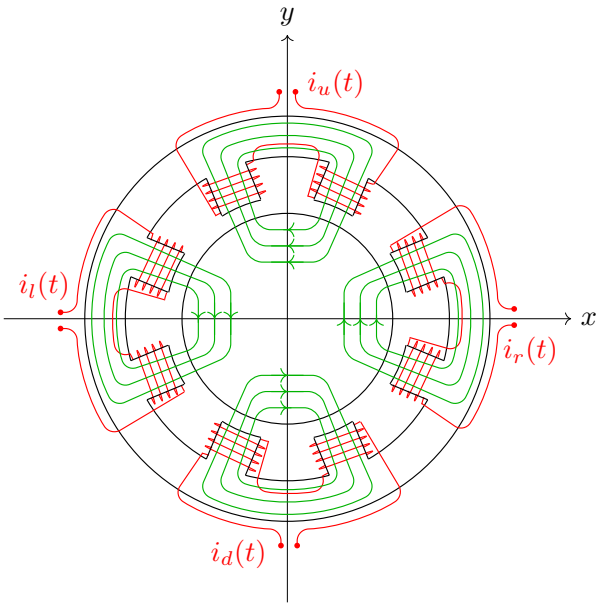

Figure 1: 8-pole Magnetic Bearing

As one can see in Figure 1, this configuration has uncoupled magnetic fluxes (represented in green). The following development is based on references such as [6, 2]. A position control scheme can be implemented independently – one for the x direction and one for the y – due to electromagnets' symmetry.

Reluctance forces equations rely on two control variables – $i_l(t)$ and $i_r(t)$, for the x direction; $i_u(t)$ and $i_d(t)$, for the y. This situation can be problematic in a control point of view. Differential currents approach may be applied so that $i_x(t)$, or $i_y(t)$, will be the only control variables [7].

The resulting equations are nonlinear, but considering that the bearing operates near the operating point ($i_x(t) \approx x(t) \approx 0$) under normal conditions, Taylor series can be applied, which allows a linearization of the proposed model for the x direction. Likewise, the same procedure

is done for the y.

The linearized reluctance forces for the 8-pole AMB are presented in (1):

$$F_x(t) = g_p x(t) + g_i i_x(t) \qquad \text{and} \qquad F_y(t) = g_p y(t) + g_i i_y(t) \tag{1}$$

where

$$g_p = \frac{\mu_0 N_a^2 A_a i_b^2}{h^3} \qquad \text{and} \qquad g_i = \frac{\mu_0 N_a^2 A_a i_b}{h^2} \tag{2}$$

are the magnetic constants.

A more compact geometry, allowing a cheaper structure and more space for heat dissipation, called 4-pole Magnetic Bearing, is being used in many applications [8, 9]. Consider a 4-pole Magnetic Bearing shown in Figure 2. The following concepts are based on [6].

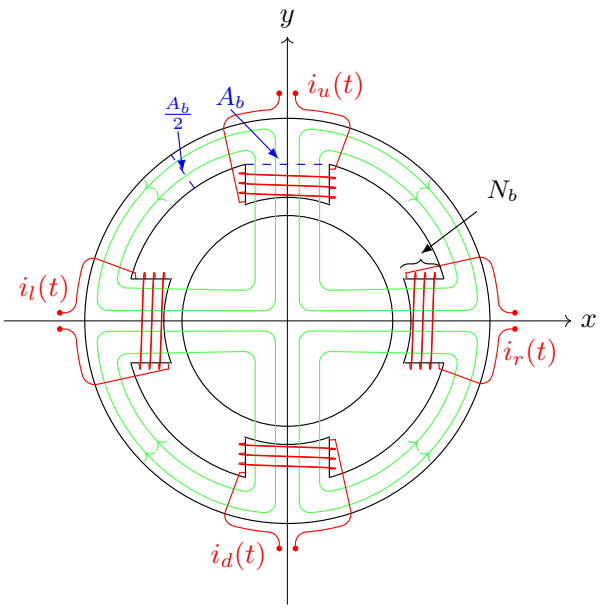

Figure 2: 4-pole Magnetic Bearing

The main difference between the 8-pole and 4-pole geometries is that the latter has an interconnection of magnetic fluxes [10]. It is important to mention that the symmetry detected in an 8-pole Magnetic Bearing is kept here. The same mathematical procedure to obtain the reluctance forces may be developed, but now taking into account the fluxes interconnection.

One may notice in Figure 3 the interconnected magnetic flux distribution caused by current $i_r(t)$. The notation ϕ_{mn} refers to the magnetic flux that crosses the m pole due to the current that circulates at the n pole. The reluctance forces in this geometry rely on the total magnetic flux ϕ_m (for each pole m) which is a function of the partial fluxes ϕ_{mn}, as can be seen in (3):

$$\begin{aligned} \phi_r &= \phi_{rr} + \phi_{ru} - \phi_{rl} + \phi_{rd} \qquad & \phi_u &= -\phi_{ur} - \phi_{uu} - \phi_{ul} + \phi_{ud} \\ \phi_l &= -\phi_{lr} + \phi_{lu} + \phi_{ll} + \phi_{ld} \qquad & \phi_d &= -\phi_{dr} + \phi_{du} - \phi_{dl} - \phi_{dd} \end{aligned} \tag{3}$$

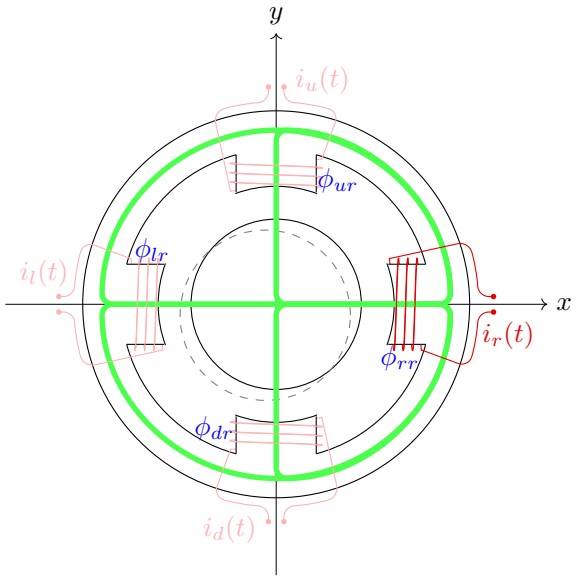

Figure 3: 4-pole interconnected magnetic flux distribution associated only with the current $i_r(t)$

A step by step mathematical development can be seen in [6]. The linearized reluctance forces for the 4-pole AMB are presented in (4):

$$F_x(t) = g_p x(t) + g_i i_x(t) \qquad \text{and} \qquad F_y(t) = g_p y(t) + g_i i_y(t) \tag{4}$$

where

$$g_p = \frac{2\,\mu_0\,N_b^2\,A_b\,i_b^2}{h^3} \qquad \text{and} \qquad g_i = \frac{2\,\mu_0\,N_b^2\,A_b\,i_b}{h^2} \tag{5}$$

are the magnetic constants. These values have an extra factor of 2 when compared to the first topology, shown in (2); this means that the magnetic constants of a 4-pole AMB are, at least, 2 times higher than in the 8-pole case.

Although this geometry uses interconnected fluxes, the reluctance forces are decoupled from each other, as demonstrated in (4).

An even more compact structure, the 3-pole AMB, has been studied over the past few years [2, 5]. Consider a 3-pole AMB in an optimal configuration shown in Figure 4. In this design, we shall consider a horizontal rotor being supported by the device. This scheme has the minimum number of poles able to balance the rotor, allowing a better heat dissipation and lower iron losses [11, 5].

In this asymmetric configuration (due to the odd number of poles), it is possible to use one less actuator as two poles share the same coil wiring [11, 12]. The modelling process is very similar compared to the other geometries but interesting since an odd number of poles causes a disbalancing in the reluctance forces. One may notice in Figure 5 the interconnected magnetic flux distribution caused by current $i_1(t)$. The total magnetic flux ϕ_m (for each pole m) is a

function of the partial fluxes ϕ_{mn}, as can be seen in (6):

$$\begin{aligned} \phi_1 &= \phi_{11} + \phi_{12} + \phi_{13} \qquad \phi_2 = -\phi_{21} - \phi_{22} + \phi_{23} \\ &\qquad\qquad\qquad\quad \phi_3 = -\phi_{31} + \phi_{32} - \phi_{33} \end{aligned} \tag{6}$$

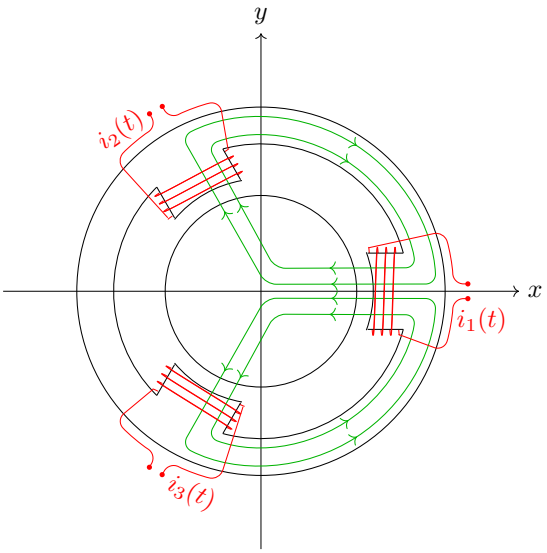

Figure 4: Optimal configuration of a 3-pole Magnetic Bearing

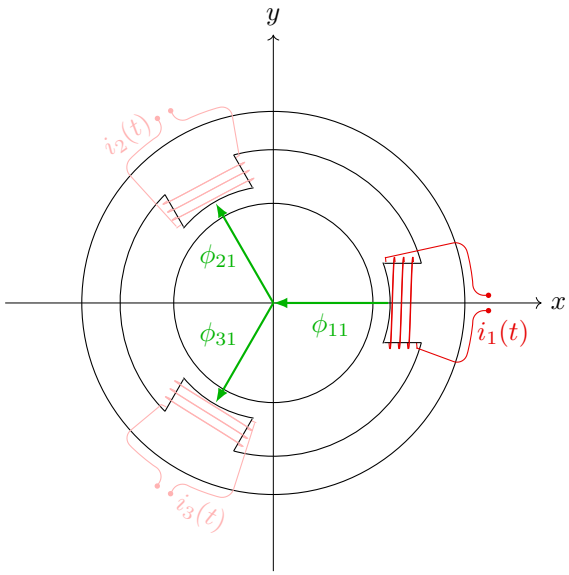

Figure 5: 3-pole interconnected magnetic flux distribution associated only with the current $i_1(t)$

A step by step mathematical development can be seen in [13, 11, 2]. The linearized reluctance forces for the 3-pole AMB are presented in (7):

$$F_x(t) = \frac{1}{2} g_p x(t) + \frac{\sqrt{3}}{3} g_i i_{d3} \qquad \text{and} \qquad F_y(t) = \frac{1}{2} g_p y(t) + g_i i_{d1} \tag{7}$$

where

$$g_p = \frac{\mu_0 \, N_c^2 \, A_c \, i_{B1}^2}{h^3} \qquad \text{and} \qquad g_i = \frac{\mu_0 \, N_c^2 \, A_c \, i_{B1}}{h^2} \tag{8}$$

are the magnetic constants. It is not straightforward to compare the 3-pole AMB reluctance forces to the other results, since the differential currents are not restricted to just one axis. However, keeping the currents in the same magnitude order, the reluctance forces in the 3-pole AMB are lower than those of 8-pole and 4-pole AMBs.

State space models are an important tool, considering a later application of a linear control technique. The dynamic analysis considers a rigid and homogeneous shaft. Further details are presented in [1, 2, 10].

The first two geometries (8-pole and 4-pole AMBs) share the same model pattern. State space representation is shown in (9):

$$\dot{\boldsymbol{x}}(t) = A\boldsymbol{x}(t) + B\boldsymbol{u}(t) + D\boldsymbol{v}(t) \tag{9}$$

where the matrices A, B and D have structures defined in (10):

$$A = \begin{bmatrix} 0 & I \\ A_{21} & A_{22} \end{bmatrix} \qquad B = \begin{bmatrix} 0 \\ B_2 \end{bmatrix} \qquad D = \begin{bmatrix} 0 \\ D_2 \end{bmatrix} \tag{10}$$

where the blocks A_{21}, A_{22}, B_2 and D_2 are 2×2 matrices that depend on the constructive parameters of the existing prototypes [1, 2, 10]; block A_{22} depends on the rotor speed. The prototypes are equipped with sensors that measure the rotor position in two orthogonal directions: x_s and y_s. These signals, together with the corresponding velocities, are the state vector components, as shown in (11):

$$\boldsymbol{x} = \begin{bmatrix} x_s \\ y_s \\ \dot{x}_s \\ \dot{y}_s \end{bmatrix} \qquad \boldsymbol{u} = \begin{bmatrix} i_x \\ i_y \end{bmatrix} \qquad \boldsymbol{v} = \begin{bmatrix} \cos\,(\omega t) \\ -\sin\,(\omega t) \end{bmatrix} \tag{11}$$

The control vector $\boldsymbol{u}$ components are the differential currents injected in the AMB coils. An extra (small) mass can be attached to the rotor of the examined prototypes; this allows the study of unbalanced masses in the rotational dynamics. The net effect of this lack of symmetry is the appearance of the harmonic disturbances in vector $\boldsymbol{v}$ that enter the model through D.

A different procedure must be done for the 3-pole AMB as the reluctance forces are different and the torque from gravitational force should be taken into account since the rotor is in the horizontal position. The standard state space representation shown in (9) and matrices presented in (10) are valid here as well.

The state space vector $\boldsymbol{x}$, control inputs $\boldsymbol{u}$ and disturbance vector $\boldsymbol{v}$ are chosen to be the ones shown in (12):

$$\boldsymbol{x} = \begin{bmatrix} x_s \\ y_s \\ \dot{x}_s \\ \dot{y}_s \end{bmatrix} \qquad \boldsymbol{u} = \begin{bmatrix} \frac{\sqrt{3}}{3} i_{d3} \\ i_{d1} \end{bmatrix} \qquad \boldsymbol{v} = \begin{bmatrix} \cos(\omega t) \\ -\sin(\omega t) \end{bmatrix} \tag{12}$$

As we are working with an approximate linear model, these equations are accurate only around the operation point. Besides that, one can represent this as a linear and time-invariant system if and only if a constant value is fixed for ω.

Some control strategies can be used in an AMB system, such as PID [14], pole placement technique [15] and $\mathcal{H}_\infty$ regulator [16]. This paper addresses the use of an optimal control strategy based on Linear Quadratic Regulator (LQR) theory [1, 17, 18].

Consider a block diagram, in Figure 6, that illustrates a full state feedback. The controller's goal is to drive the closed-loop poles to a desired position, stabilizing the rotor.

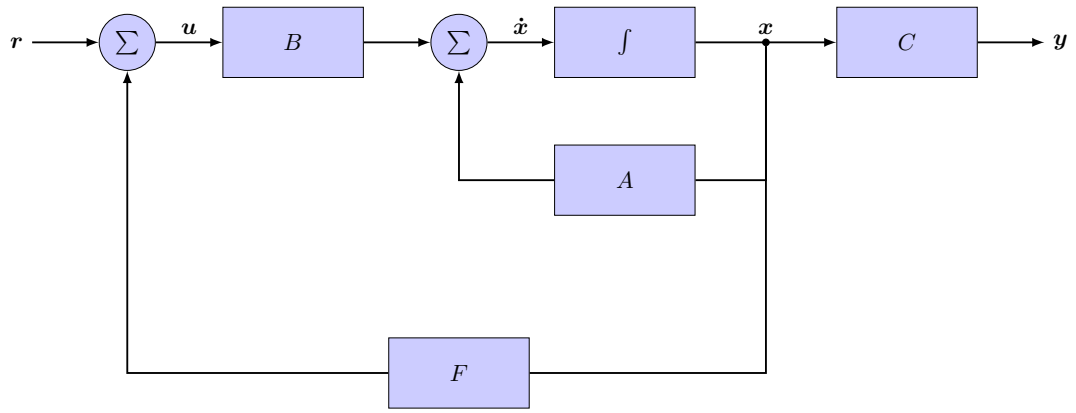

Figure 6: Full state feedback block diagram

LQR control has an advantage, compared to pole placement technique, of providing a systemic and automatic procedure to calculate the feedback gain matrix [17]. LQR perfomance index J is defined by two quadratic functions and can be expressed by (13):

$$J = \int_0^\infty \left(\boldsymbol{x}^T(t) Q \boldsymbol{x}(t) + \boldsymbol{u}^T(t) R \boldsymbol{u}(t)\right) \mathrm{d}t \tag{13}$$

where the weighting matrix Q (state error) is symmetric positive semidefinite and the weighting matrix R (energy consumption) is symmetric positive definite.

Considering a controllable system and that all states are observable and available (here x and y are measured and $\dot{x}$ and $\dot{y}$ are estimated), we can write (14):

$$\boldsymbol{u^*} = F^* \boldsymbol{x} \tag{14}$$

where $\boldsymbol{u^*}$ is the optimal control law that minimizes J, through the feedback gain matrix F^*, given by (15):

$$F^* = -R^{-1} B^T P \tag{15}$$

in which P is the solution of an algebraic matrix Riccati equation, as can be seen in (16):

$$A^T P + PA - PBR^{-1}B^T P + Q = 0 \tag{16}$$

In this work, three LQR control techniques are designed and simulated. The first one, named here as centralized LQR (LQRc), refers to the "traditional" LQR, where all states are fedback and interact with each other, which can be seen in (17):

$$\boldsymbol{u} = F_c^* \boldsymbol{x} \implies \begin{bmatrix} u_1 \\ u_2 \end{bmatrix} = \begin{bmatrix} f_{11} & f_{12} & f_{13} & f_{14} \\ f_{21} & f_{22} & f_{23} & f_{24} \end{bmatrix} \boldsymbol{x} \tag{17}$$

In most cases, all F_c^* (centralized) matrix elements are nonzero, since there is a well-defined connection between every single state. This leads to a greater computational effort.

An alternative and interesting solution would be the presence of some zero elements in the feedback gain matrix, as this would alleviate the control implementation. This is possible using the decentralized Linear Quadratic Regulator (LQRd). In a gain matrix F_d^* (decentralized), each one of the two input variables is decoupled and independent of the other. That is to say, each input is related only to an output and its derivative, as shown in (18):

$$u_1 = f_{11} x_s + f_{13} \dot{x}_s \qquad \text{and} \qquad u_2 = f_{22} y_s + f_{24} \dot{y}_s \tag{18}$$

Further details are presented in [7, 19]. The decentralized structure can be expressed by (19):

$$\boldsymbol{u} = F_d^* \boldsymbol{x} \implies \begin{bmatrix} u_1 \\ u_2 \end{bmatrix} = \begin{bmatrix} f_{11} & 0 & f_{13} & 0 \\ 0 & f_{22} & 0 & f_{24} \end{bmatrix} \boldsymbol{x} \tag{19}$$

The necessary conditions for F to satisfy (19) and minimize J in (13) are in [19, 20]; they lead to an algorithm that will be used in the sequel.

The work developed in [19] comes up with an even more particular structure. As it relies on two parameters, this control law is called two-parameter decentralized Linear Quadratic Regulator ($\text{LQRPD}_{2\text{p}}$). Similar to the previous case, input variables are decoupled, taking into account only their position and speed on the interest direction. The difference here is that an additional restriction is imposed on the control law, making it simpler. The $\text{LQRPD}_{2\text{p}}$ structure is as follows:

$$\boldsymbol{u} = F_{2p}^* \boldsymbol{x} \implies \begin{bmatrix} u_1 \\ u_2 \end{bmatrix} = \begin{bmatrix} p & 0 & d & 0 \\ 0 & p & 0 & d \end{bmatrix} \boldsymbol{x} \tag{20}$$

Only two parameters appear in the feedback matrix: p for the x_s and y_s and d for the derivatives. All the existence conditions for this problem, as well as an algorithm leading to the solution can be found in [19]. These results will be used in the next section, but will be not presented here.

3 Results

The magnetic constants g_p and g_i are determined using the prototype' geometric parameters [6, 10], in addition to the base current i_b (8-pole and 4-pole) or i_{B1} (3-pole).

Considering $i_b = i_{B1} = 0.52$ A [2], the first simulation set is performed, comparing all three geometries in different control schemes. The operating speed ω used is 21 rad/s (approximately 200 rpm), 356 rad/s (about 3400 rpm) and 942 rad/s (roughly 9000 rpm). Figure 7 shows the centralized LQR response for each speed and geometry.

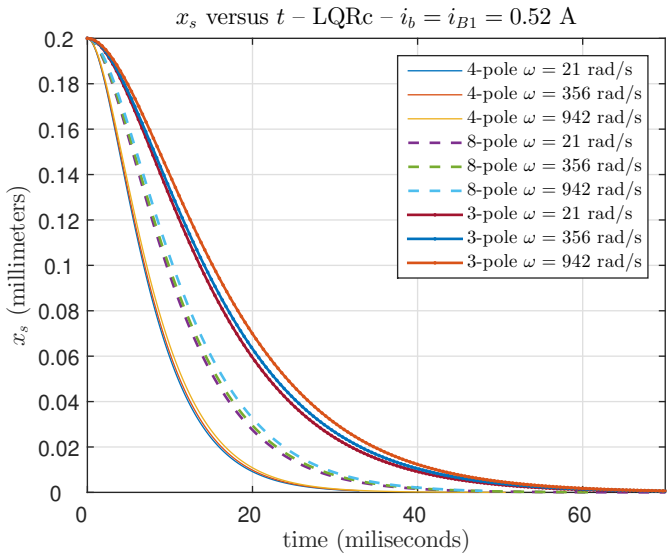

Figure 7: Centralized LQR response

As can be seen, the 4-pole AMB is the fastest to return to equilibrium. In second place, comes out the 8-pole Magnetic Bearing, and finally the 3-pole. However, when the rotor operating speed is increased from 200 rpm to 3400 rpm (and after from 3400 rpm to 9000 rpm), we have a slightly longer settling time – this is noticed in all geometries. Four-pole geometry settling time variations (after increasing the operating speed ω) are much smaller than the others, as can be seen in Figure 7 and in Table 1.

Table 1: Comparison between LQRc, LQRd and LQRPD_{2p}: settling time – $i_b = i_{B1} = 0.52$ A

Settling time (in ms) – $i_b = i_{B1} = 0.52$ A			
	$\omega = 21$ rad/s	**$\omega = 356$ rad/s**	**$\omega = 942$ rad/s**
LQRc	8-pole: 42.9 4-pole: 30.8 3-pole: 61.7	8-pole: 43.9 4-pole: 31.3 3-pole: 63.6	8-pole: 45.2 4-pole: 32.0 3-pole: 65.3
LQRd	8-pole: 43.0 4-pole: 30.9 3-pole: 61.8	8-pole: 44.1 4-pole: 31.6 3-pole: 64.6	8-pole: 44.7 4-pole: 32.9 3-pole: 70.3
LQRPD_{2p}	8-pole: 42.7 4-pole: 30.6 3-pole: 61.3	8-pole: 40.0 4-pole: 29.4 3-pole: 56.0	8-pole: 36.2 4-pole: 27.3 3-pole: 50.7

For the decentralized LQR control strategy, a similar simulation is done, as can be noticed in Figure 8.

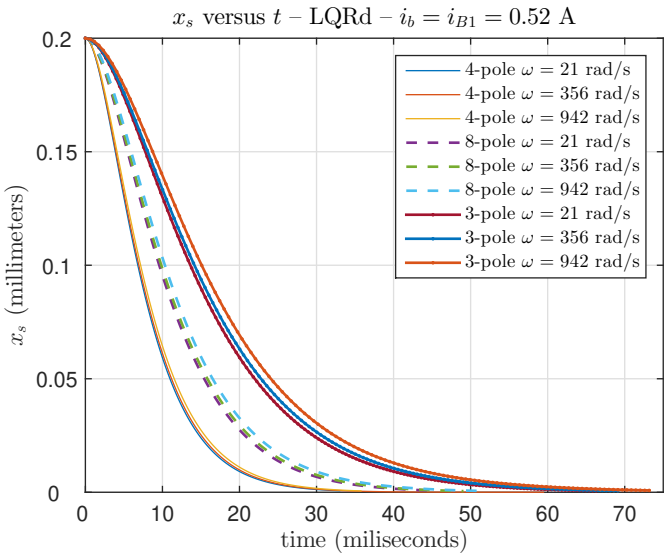

Figure 8: Decentralized LQR response

When one compares LQRc to LQRd response, the latter presents a small decrease in the eigenvalues' real part (the only exception is the 8-pole AMB with $\omega = 942$ rad/s) – therefore, a minimal settling time increase is expected in this control strategy, as exposed in Table 1.

The last control method to be simulated is the two-parameter decentralized LQR ($\text{LQRPD}_{2\text{p}}$). Figure 9 exhibits its response.

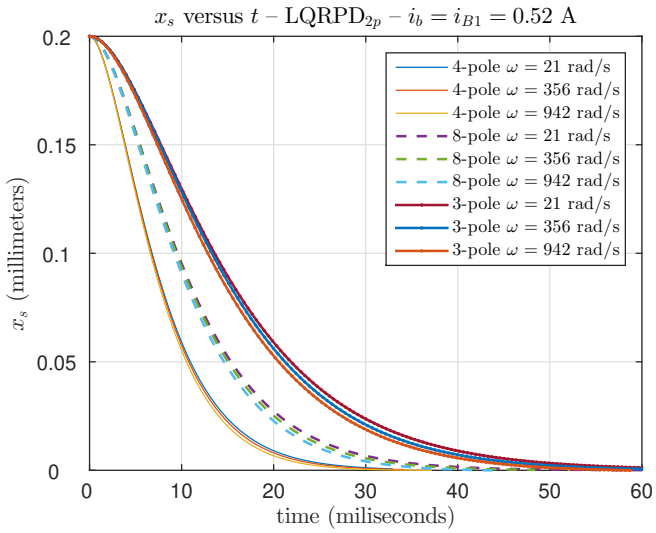

Figure 9: Two-parameter decentralized LQR response

Similarly to LQRc and LQRd strategies, the 4-pole AMB is the one that returns faster to the center position (regardless of ω), followed by the 8-pole, and finally the 3-pole geometry. In this strategy, one can see, in Table 1, a shorter settling time, for all geometries and ω. In fact, $\text{LQRPD}_{2\text{p}}$ control strategy provides an optimal gain matrix, and the closed-loop system response is fast enough. Notice that as the rotor speed increases, the centralized and decentralized strategies present a longer settling time, whereas in the $\text{LQRPD}_{2\text{p}}$ case this time decreases.

In order to compare the prototype's performance against disturbances, a 1 gram unbalance mass is placed on the rotor, causing an orbital motion due to the appearance of harmonic forces. Hence, x_s would not go to zero, unlike Figure 7 (where disturbances were not considered), for example.

Each control strategy is compared, in order to analyze a given AMB geometry. For the centralized LQR, considering a low rotation speed, Figure 10a shows x_s by y_s curves for the eight, four and three-pole geometries. It can be seen that the orbital motions for the 4-pole geometry are smaller than the 8-pole, which are smaller than the 3-pole. The lower are the orbital movements, the more rigid is the suspension, featuring a better performance against disturbances.

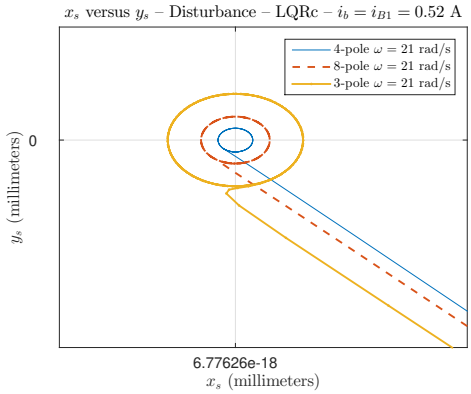

(a) Centralized LQR

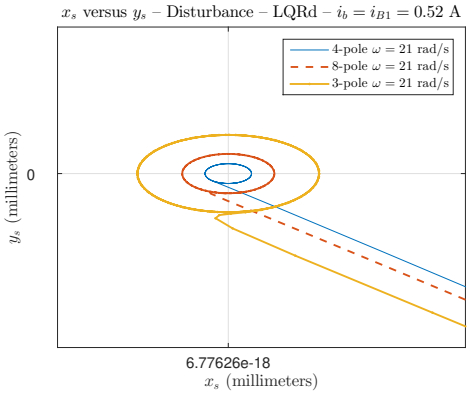

(b) Decentralized LQR

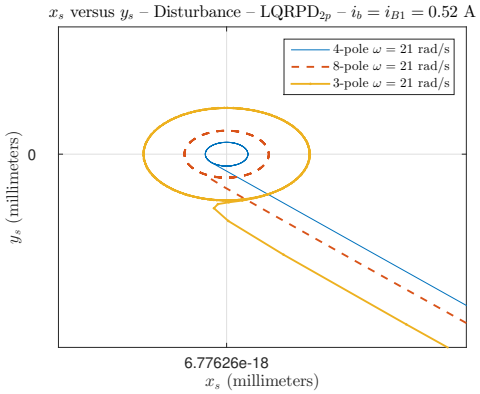

(c) Two-parameter decentralized LQR

Figure 10: Orbital motion – $\omega = 21$ rad/s

For the decentralized LQR (Figure 10b) and the two-parameter decentralized LQR (Figure 10c) cases, it is clear that the response curves, in the three control strategies, are nearly the same, given the low rotation speed.

With the increase of the rotation speed to 356 rad/s, it is apparent the higher influence of harmonic forces on the x_s and y_s response curves. This happens because the torque caused by the unbalance mass depends on the square of the rotor speed. Nevertheless, the 4-pole AMB is the one with the best performance, as can be seen in Figure 11a.

The same comments made, when considering the speed of 21 rad/s, are valid here. When looking at Figure 11b, the decentralized control strategy does not show any difference in the orbital motion, when compared to the centralized control. In a like manner, the two-parameter decentralized control (Figure 11c) displays a very similar response due to disturbances.

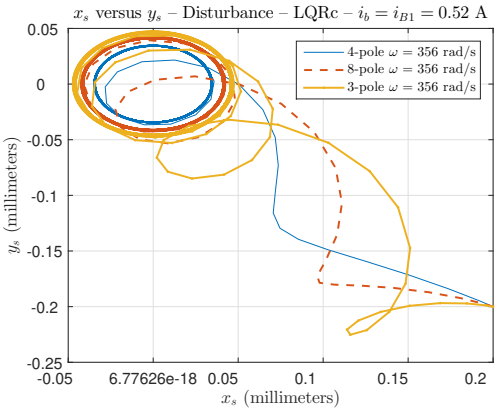

(a) Centralized LQR

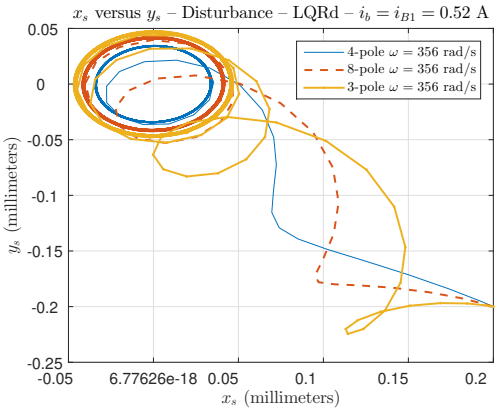

(b) Decentralized LQR

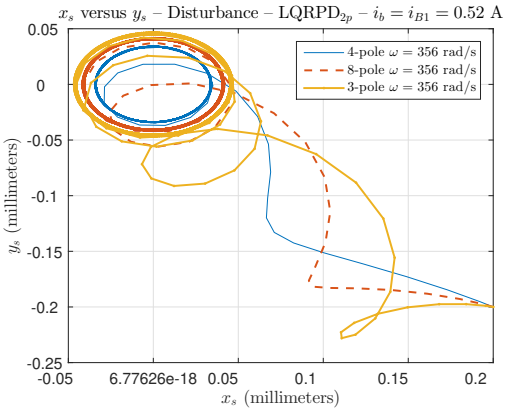

(c) Two-parameter decentralized LQR

Figure 11: Orbital motion – $\omega = 356$ rad/s

Another important fact concerns the number of iterations necessary to stabilize the system: the two-parameter decentralized strategy proved to be equally or more effective in almost all simulations and geometries (7 out of 9 cases). Table 2 shows this fact.

Table 2: Comparison between LQRd and LQRPD$_{2p}$: number of iterations – $i_b = i_{B1} = 0.52$ A

Number of iterations – $i_b = i_{B1} = 0.52$ A			
	$\omega = 21$ rad/s	**$\omega = 356$ rad/s**	**$\omega = 942$ rad/s**
LQRd	8-pole: 2 4-pole: 8 3-pole: 2	8-pole: 6 4-pole: 11 3-pole: 8	8-pole: 15 4-pole: 15 3-pole: 28
LQRPD$_{2p}$	8-pole: 3 4-pole: 2 3-pole: 3	8-pole: 5 4-pole: 4 3-pole: 5	8-pole: 8 4-pole: 6 3-pole: 10

With what has been shown so far in this paper, it seems that the two-parameter decentralized control strategy is the best of all simulated. In order to analyze the control signal of the three strategies, another simulation is performed, using as reference the 4-pole geometry and a rotor speed of 356 rad/s. This choice is justified by the fact that the 4-pole AMB is the one with the shortest settling time and the most rigid suspension among all studied. Thus, it is interesting to analyze how the control signal varies over time for this geometry. Moreover, an average operating speed ($\omega = 356$ rad/s) is adopted, since, as presented in the simulations, changing ω does not significantly change the settling time.

As the LQRPD$_{2p}$ was the one that presented the shortest settling time of all strategies, it is interesting to note whether this good transient response requires a greater control effort when compared to other LQR techniques, as shown in Figure 12.

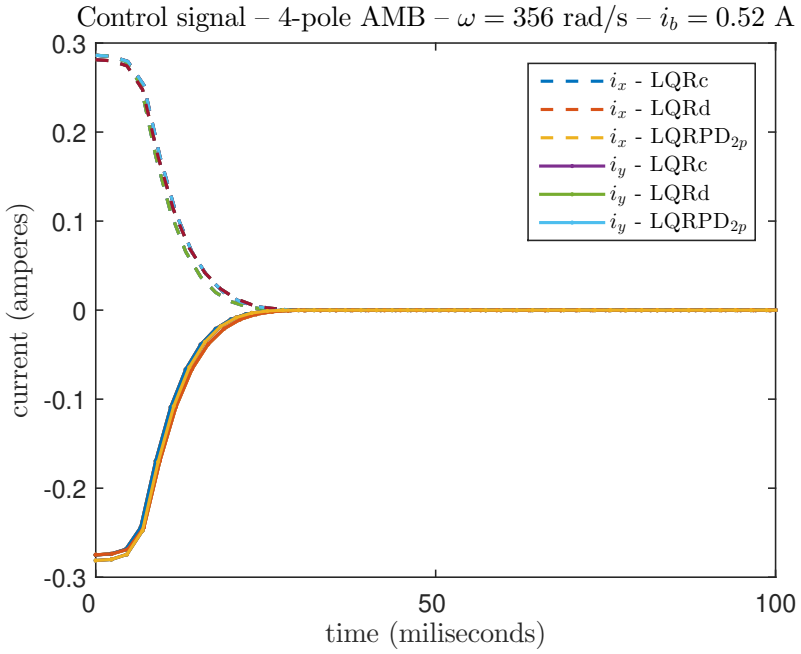

Figure 12: 4-pole Magnetic Bearing control signal

Immediately, one notices that the electric currents i_x and i_y (that is, the control signal) necessary to stabilize the 4-pole AMB are approximately equal to 0.28 A. This represents about 54% of the base current used (0.52 A). Another fact to be highlighted is that the three curves (for each axis) are basically superimposed. Although the two-parameter decentralized strategy has the shortest settling time, no additional control effort is required.

4 Conclusions

We have shown that the 4-pole Magnetic Bearing was the fastest (or equally fast) geometry, followed by the eight, and finally the three-pole AMB. The two-parameter decentralized Linear Quadratic Regulator ($\text{LQRPD}_{2\text{p}}$) is a viable alternative, as it presents a structure with only two different parameters, with total decoupling between the variables. Besides that, two-parameter decentralized LQR presented the shortest settling time among all strategies and the lowest number of iterations in 77.8% of the cases, with the same control effort compared to the other strategies. An increase in ω leads to a longer stabilization time (the exception is the two-parameter decentralized strategy, in which there is a reduction in this settling time). Furthermore, simulations with harmonic disturbances were made, and revealed that the change in the control strategy does not impact these results – in all simulations, the 4-pole AMB was the one with the best results. It should be mentioned that in these comparisons the 3-pole AMB had an horizontal rotor while the other geometries used a vertical one. Further research is needed for the case of all structures holding rotors in the same position, be it vertical and/or horizontal.

References

[1] R. M. Stephan, F. C. Pinto, A. C. D. Gomes, J. A. Santisteban, and A. O. Salazar, *Mancais Magnéticos - Mecatrônica sem atrito*. Editora Ciência Moderna Ltda., 1 edição ed., 2013.

[2] V. R. Vasco, "Modelagem e controle ótimo de um mancal magnético de três polos," Master's thesis, COPPE/UFRJ, 2019.

[3] W. Jones, "Earnshaw's theorem and the stability of matter," *Eur. J. Phys 1*, pp. 85–88, 1980.

[4] A. CHIBA, T. FUKAO, and e. ICHIKAWA, O., *Magnetic Bearings and Bearingless Drives*. Newnes-Elsevier, 2005.

[5] W. Zhang and H. Zhu, "Radial magnetic bearings: An overview," *Results in Physics*, 2017.

[6] P. H. S. Pinto, "Comparações teóricas e práticas sobre geometrias de mancais magnéticos," Master's thesis, COPPE/UFRJ, 2018.

[7] G. Schweitzer, H. Bleuler, and A. Traxler, *Active Magnetic Bearings*. vdf Hochschulverlag, 1994.

[8] J. M. Krodkiewski and R. B. Zmood, "Use of programmed magnetic bearing stifness and damping to minimize rotor vibrations," *ISMB*, 1992.

[9] K. Kjolhede and I. F. Santos, "Experimental contribution to high-precision characterization of magnetic forces in active magnetic bearings," *Gas Turbines: Structures and Dynamics*, 2006.

[10] D. F. B. David, J. S. Santisteban, and A. C. D. Gomes, "Modeling and testing strategies for an interconnected four-pole magnetic bearings," *Actuators*, 2017.

[11] S. Chen and C. Hsu, "Optimal design of a three-pole active magnetic bearing," *IEEE Transactions on Magnetics*, 2002.

[12] S. Chen, S. Chen, and S. Yan, "Experimental validation of a current-controlled three-pole magnetic rotor-bearing system," *IEEE Transactions on Magnetics*, 2005.

[13] D. F. B. David, J. S. Santisteban, A. C. D. Gomes, and V. R. Vasco, "Considerations on the mechanical dynamics of interconnected flux three-pole magnetic bearings," *ISMB*, 2018.

[14] R. R. Gomes, "Motor mancal com controle implementado em um dsp," Master's thesis, COPPE/UFRJ, 2007.

[15] G. Schweitzer and E. H. Maslen, *Magnetic Bearings*. Springer-Verlag Berlin Heidelberg, 2009.

[16] A. R. FRANCO, "Posicionamento de eixo com motor mancal magnético utilizando controle h-infinito," Master's thesis, COPPE/UFRJ, 2013.

[17] K. Ogata, *Engenharia de Controle Moderno*. Pearson, 2011.

[18] N. S. Nise, *Engenharia de Sistemas de Controle*. LTC, 2017.

[19] L. S. Rodrigues, "Controle ótimo descentralizado a dois parâmetros para mancais-motores magnéticos," Master's thesis, COPPE/UFRJ, 2005.

[20] H. Bleuler, *Decentralized control of magnetic rotor bearing systems*. Doctor of technical sciences dissertation, Swiss Federal Institute of Technology, Zurich, 1984.